Combustion and Flame 211 (2020) 430–444

Contents lists available at ScienceDirect

Combustion and Flame

journal homepage: www.elsevier.com/locate/combustflame

Quantifying soot nanostructures: Importance of image processing parameters for lattice fringe analysis

Sebastian A. Pfau[a,*], Antonino La Rocca[a], Michael W. Fay[a,b]

[a] Department of Mechanical Materials and Manufacturing Engineering, University of Nottingham, University Park, Nottingham NG7 2RD, UK
[b] Nanoscale and Microscale Research Centre, University of Nottingham, University Park, Nottingham NG7 2RD, UK

ARTICLE INFO

Article history:
Received 20 May 2019
Revised 9 October 2019
Accepted 11 October 2019

Keywords:
Carbon nanostructure
Lattice fringe analysis
Particulate matter
Soot
Transmission electron microscopy

ABSTRACT

Fringe analysis is a commonly used method to quantify soot nanostructures. However, the settings of the involved filters and their impact on the results are rarely addressed. In this study, the influence of the three filter parameters as well as two aspects of the image acquisition was assessed experimentally. For the analysis, a carbon black as well as one diesel engine and one gasoline direct injection (GDI) engine soot sample were used. Gaussian low-pass filter standard deviations larger 1.5 yielded only minor differences in fringe metrics. Standard deviations between 2.0 and 3.0 enabled realistic representation of fringes. A linear correlation was found between the white top-hat transformation disk size and all fringe analysis metrics. For realistic nanostructure representation, disk sizes of 5 px and 7 px are most suitable. Threshold values as calculated by Otsu's method generally yielded the best nanostructure representation. Any deviation distorted the extracted fringes and noticeably reduced their total number. Thus, consistent use of Otsu thresholds without alterations is advised. Deviating from the neutral electron microscope focus point by under- and over-focusing resulted in distinctive drops in both fringe lengths and Otsu thresholds. Consistent focusing with the help of fast Fourier transformations of the respective particles is vital for reliable results. The effect of reduced noise levels by repeated averaged images was found to be minor beyond the model of the camera used. The region of interest size correlated linearly with the number of extracted fringes, however, it did not affect the fringe metrics. For statistically reliable analysis, a minimum of 4000 fringes is suggested. The GDI sample exhibited the shortest fringes and the highest tortuosity. For diesel soot and carbon black, similar fringe lengths could be observed. The highest tortuosity was found for GDI soot, followed by diesel soot and carbon black.

1. Introduction

Accurate characterization of airborne particulate matter and particularly soot has increasingly gained interest in recent years. This can be attributed to their impact on human health as a cancerous substance [1,2], but also the effect on other organisms such as in marine environments [3]. Moreover, implications on climate due to light absorption and scattering are being repeatedly highlighted [4,5]. Generally, the formation of soot is associated with the incomplete combustion of hydrocarbon fuels in non-stoichiometric, fuel-rich conditions [6,7]. Fuel pockets within fuel–air mixtures give rise to initial radical and unsaturated species [8]. Subsequent growth processes lead to the formation of primary particles and eventually larger agglomerates. The specific properties of the generated soot depend highly on a variety of parameters. These can be found for example in different types and compositions of fuel [9–11], varying fuel–air-ratios [12,13] or fuel flow rates [14,15]. For internal combustion engines, the particulate matter emissions are widely influenced by operating conditions such as injection modes [16,17], cold start conditions [18,19] or engine speed and load [18,20,21].

While particulate matter from diesel engines is a rather well-covered subject, such emissions have only recently increased for gasoline engines with the introduction of direct injection systems [22]. To safeguard humans, the issue of soot emissions has commonly been combated for diesel cars with particulate filters. The soot is trapped in layers of mesh grid, accumulates in the filter and is periodically oxidized, commonly referred to as regeneration. For optimal efficiency, the mesh grade, as well as the regeneration frequency, has to be adjusted to the specific soot properties. Importance comes mostly to the size of agglomerates and primary particles, as well as to the particle nanostructure. While the former can

---

[*] Corresponding author.
E-mail address: sebastian.pfau@nottingham.ac.uk (S.A. Pfau).

https://doi.org/10.1016/j.combustflame.2019.10.020

affect the build-up within the filter and surface area [23,24], the latter provides information on active carbon edge sites and reactivity [25,26]. Such information is highly relevant for other areas, as soot also transfers into the lubricating oil via the oil film on the cylinder walls and piston blow-by gases [27]. Increasing concentrations of soot particulates in the lubricating oil have been found to alter its viscosity [28]. This can affect the performance of components with thin oil films, e.g. valve trains [29], and thus overall engine performance. Moreover, the nanostructure has been suggested to influence the interaction with the oil additives and alter the anti-wear properties of the oil [30]. Recent studies indicate that the soot formed in gasoline direct injection engines exhibits differences to its diesel counterpart [31,32]. Therefore, effective characterization tools for soot and its nanostructure are required to enable the design of suitable products, such as particulate filters and lubricating oils.

Established techniques for nanostructure characterization can be found in Raman spectroscopy and X-ray diffraction (XRD). The former can identify nanostructure types, such as ordered graphitic, disordered graphitic, and amorphous carbon domains. However, due to differences in the experimental parameters (i.e. laser wavelength, laser intensity, and spectra collection time) and the band fitting (i.e. the number of bands for deconvolution), only relative comparisons within studies are made. XRD can provide lattice spacing numbers of the sample structure. Both techniques provide general information on the sample by assessing larger sample regions in comparison to the size of individual particles. In contrast, transmission electron microscopy (TEM) enables the imaging of individual soot agglomerates and primary particles using various magnifications, up to the atomic level. Thus, the technique can provide a wide range of different properties and more nuanced information. Particular areas and specific regions can be easily differentiated. Therewith detailed information on both morphology and nanostructure can be obtained.

The observable soot morphology provides initial information about the general appearance and type of soot. This can range from larger particles in clusters of several hundred nanometers as commonly observed for carbon blacks, to small and “sludge-like” particulates as observed for some gasoline direct injection (GDI) soot samples [31,32]. Moreover, simple measurements of primary particle size and two-dimensional agglomerate dimensions can be carried out without extensive software or image acquisition procedures. However, two-dimensional images cannot fully capture the fractal, three-dimensional nature of soot agglomerates. Recent advances towards electron tomography [33] and its automation [34] could provide a feasible way to close this gap.

In addition to morphological imaging at low resolution, higher resolutions can be utilized to capture the particle nanostructure. Early attempts of manual measurements from electron microscopy images have been performed as early as 1971 [35]. The individual segments of graphitic layers, commonly referred to as fringes, can be assessed for their geometric parameters (referred to as metrics in the following), i.e. fringe length, tortuosity, and separation. The length of the fringe is defined as the distance between its endpoints along the fringe, i.e. geodesic length. The shape of fringes can be quantified as tortuosity by obtaining the ratio of the respective geodesic length and the direct endpoint distance, i.e. Euclidian length. Lastly, the separation between fringes can provide details on the graphitic layer spacing. Several years after the initial advances, various researchers moved towards automated analysis of high-resolution TEM images [36–39]. More recently, a comprehensive methodology was developed by Yehliu et al. [40] and implemented using the commercial software MATLAB®. Their approach was subsequently widely adopted in the literature [41–44]. However, other approaches of fringe analysis can be found in the existing literature [45–50].

Despite differences between the specific methods, some recurring elements can be identified across the techniques. Initially, histogram equalization is employed to expand distribution of intensities over the full grayscale. Thus, the contrast of fringes to the background is enhanced. To reduce both residual noise and noise from the histogram equalization, low-pass filters are applied. While initial approaches employed ideal filters [37], Gaussian filters in the frequency domain have been used in later studies to avoid resulting ringing effects [51,52]. Despite correction for uneven illumination of the TEM before the acquisition of images [53], white top-hat transformation is often included to filter any artifacts from remaining illumination variations [40]. Subsequently, fringes can be extracted from the prepared image by threshold filtering. However, the obtained fringes require further processing to allow for automated calculations. As such, raw fringes have to be reduced to a single line of a single-pixel width by skeletonization. Moreover, branched fringes have to be resolved by splitting and subsequent connecting of similarly orientated branches. Upon completion of these steps, length and tortuosity can be obtained for each fringe. While not all of the described steps are included in every methodology, some features of specific approaches can be noted. The method by Toth et al. [46,47,51] pays particular attention to the low-pass filter selection and subsequently fringe separation. Botero et al. [54] focused on different radial regions of entire primary particles. In contrast to analysis that is limited to the graphitic shell of a particle, this method enabled identification of differences within particles as well as changes with soot maturity. A further advanced approach was developed by Pré et al. [50]. Their algorithm is based on the assessment of parallelism between fringes. Thus, it allows for fringe stacks and continuous domains to be identified as well as quantified in terms of size and separation spacing. Consequently, information on the density of the nanostructure can be obtained. This approach was subsequently employed to assess changes in nanostructure for soot of different heights above flame burners [55] as well as laser-induced heating effects [56]. Wang et al. [48,49] employed a similar method with a focus on fringe orientation and moreover characterization of branched and self-intersecting fringes.

Values obtained by fringe analysis were compared to XRD and Raman spectroscopy measurements by Yehliu et al. [57]. Samples with various degrees of oxidation were compared. The trends in fringe separation as obtained from fringe analysis and XRD were reported to be in good agreement. Similarly, a linear correlation was observed between fringe length and band intensity ratio I_G/I_D as obtained from fringe analysis and Raman spectroscopy, respectively. These findings for Raman spectroscopy were also confirmed by Pfau et al. [32]. However, the laser wavelength can affect the observed spectra and prevent comparison of results between studies [58]. Moreover, the obtained data from Raman spectra strongly depends on the method of band deconvolution [59] as well as the method of measuring peaks, e.g. peak maximum or full width at half maximum [60]. While such restrictions are known for Raman spectroscopy, only little work has been carried out for respective constraints of fringe analysis. Gaddam et al. [61] conducted a study using three parameter-cases of three different binarization threshold values. The remaining processing parameters remained constant, however, for one case the contrast enhancement was skipped. Thus, the direct impact of the threshold value could effectively only be compared between two cases. The baseline threshold value was determined by Otsu’s method. The algorithm as proposed by Otsu [62] calculates the ideal threshold value to maximize inter-class variance and minimize intra-class variance. This approach has been implemented in the fringe analysis methodology of Yehliu et al. [40]. However, alternative methods have been used to determine suitable threshold values in other works. Palotas et al. [36] suggested that the optimal threshold value maximizes the number of obtained fringes. In addition, Sharma et al. [37] and Shim et al. [38] used fixed threshold values in combination with subsequent algorithms for correction of broken or merged fringes. In contrast, Gaddam et al. [61] did not observe a statistically significant effect of different threshold values on obtained fringe lengths. This was based on two parameter-cases without variation of parameters of neither Gaussian low-pass filter nor white top-hat transformation. However, both variables could be of importance as the threshold value is only calculated after those processing steps.

Similarly to processing parameters, the variation associated with TEM imaging is only scarcely covered in the literature. Wan et al. [63] assessed the imaging process by both TEM analysis of nascent soot samples and simulated computational studies. The findings suggested that observed fringe properties could be affected by the focusing of the microscope. However, the impact of the degree of defocus on the fringe dimensions has not been studied to date. In addition to setting the focus, the TEM operator also has to correct the instrument for uneven image illumination prior to image acquisition [53]. The operator's experience can greatly affect the results of TEM imaging, as observed by Kondo et al. [64] for the imaging of primary particles. Moreover, the respective camera equipment could play a role in this process. Maximum spatial resolution as well as image acquisition time and subsequently signal-to-noise ratio could affect how clearly fringes can be imaged.

This study sets out to assess the implications of several aspects of the fringe analysis method on the obtained results. Fringe measurements were obtained for a prescribed set of values for each of the three main processing parameters: Gaussian low-pass filter standard deviation, white top-hat transformation disk size, and binarization threshold. Furthermore, fringe analysis was carried out on TEM images acquired for a range of microscope focus points. Moreover, the effect of varying image quality was simulated by cumulative image stacking. In addition to qualitative assessment, a larger number of particles was analyzed to enable a quantitative comparison. The obtained data were first analyzed for an influence of the ROI size of the individual particles on the number of extracted fringes as well as the fringe metrics. Subsequently, a direct comparison of the three samples based on the obtained fringe metrics was conducted.

2. Experimental

2.1. Sample collection and preparation

Three different types of soot were analyzed: Carbon black, turbocharged gasoline direct injection (GDI) and diesel engine soot. The flame generated carbon black is commercially available as 'Cabot Monarch 120′. The two engine soot samples were obtained from the engine oil drains of two passenger vehicles during routine maintenance services. A three-cylinder, 1.0 L GDI engine ('GDI' in the following) was used in primarily urban driving conditions for 8488 km with activated start-stop mode. The other engine sample was obtained from a 2.0 L four-cylinder diesel engine ('Diesel' in the following) that was run for 12,875 km under light-duty operating conditions.

To extract soot particulates from the used engine lubricating oil, a cleaning protocol was applied as outlined by La Rocca et al. [25]. Oil sample quantities of 2 mL were placed in several hermetically sealed centrifuge tubes. These were then placed in an ultrasonic bath at 20 °C for ten minutes to remove contaminants bonded to the soot particles. Subsequently, the tubes were placed in an Eppendorf Centrifuge 5418R at 14,000 rpm (relative centrifugal field value of 16,873 g) for 90 min at 25 °C. The centrifugal force exerted on the sample separated the soot particles from the lubricating oil due to the difference in density. Thus, the supernatant liquid phase could be carefully extracted and subsequently be replaced by an equal amount of pure n-heptane. This cycle of ultrasonic bathing, centrifugation and heptane replacement was subsequently repeated six times. Therewith, the lubricating oil fraction was increasingly replaced by n-heptane, while the soot remained almost entirely in the tube. An effective dilution ratio of 1:75,000 compared to the initial oil sample was obtained. While the sample morphology can be altered by the centrifugation cleaning procedure, the primary particle nanostructure is not affected as observed by La Rocca et al. [25].

2.2. Transmission electron microscopy

Nanostructure images of the samples were acquired by HRTEM imaging using a JEOL 2100F TEM in the Nanoscale and Microscale Research Centre (nmRC) at the University of Nottingham. The microscope was equipped with a Gatan Orius CCD camera and operated with an incident electron beam voltage of 200 kV. A magnification of 500,000× was employed and yielded a resolution of 0.025 nm/px. The TEM grids consisted of graphene oxide support film on lacey amorphous carbon on copper mesh grid.

For the acquisition of repeated images of the same primary particle, the total beam exposure time was 12.5 s for a series of six images with exposure durations of 0.5 s. The average electron rate was 1.068×10^5 electrons nm^{-2} s^{-1}, which resulted in a total electron dose of 1.335×10^6 electrons nm^{-2} for each image series. No decomposition of the sample under the electron beam was observed.

2.3. Fringe analysis

The methodology used in this study was adapted from Yehliu et al. [40] and written in MATLAB®. The region of interest (ROI) was initially selected by the user for each image and subsequently kept constant for all iterations with various processing parameters. It should be pointed out that only the graphitic layers are here being analyzed. The disordered regions, due to amorphous nature of the particle core itself or higher particle thickness towards the center disguising the nanostructure, is being excluded.

In the raw, bright-field TEM images the fringes appear dark, as the dominant contrast mechanism is due to electrons in the respective positions being scattered or absorbed due to interaction with the carbon atoms. Thus, negative transformation is initially applied to the image. The subsequent script optimizes the image so that the fringes remain as positive information (i.e. ones) on a dark background (i.e. zeros). Instead of general histogram equalization, contrast limited adaptive histogram equalization (CLAHE) was used here. Adaptive histogram equalization (AHE) divides the ROI into 64 regions (8 × 8) and determines the ideal contrast within these. This allows better consideration of local contrast requirements, however, noise levels can be significantly elevated [65]. By imposing a contrast limitation, i.e. using CLAHE, sharp peaks in the histogram of noisy homogenous areas are redistributed and noise reduced. To further reduce noise from the histogram equalization, a Gaussian low-pass filter was employed. White top-hat transformation using disk-shaped elements was included to reduce artifacts due to uneven illumination. Subsequently, the image was processed by threshold binarization. Lastly, the visible fringes were skeletonized by reducing their thickness to a single pixel.

The specific processing parameters are only scarcely reported in the literature. In the initial publication of the commonly used method by Yehliu et al. [40], a Gaussian low-pass filter standard deviation of 1.0 is used with a filter size of 11 px. Moreover, a disk-shaped white top-hat transformation element with 5 px in size was used. The threshold was calculated using Otsu's method which yielded a value of 0.1608 for the analyzed image. Similar

Table 1
Range of processing parameters for fringe analysis. Baseline value in bold.

Processing parameter	Value range						
Gaussian low-pass filter std. dev. (filter size in px)	0.5 (3)	1.0 (7)	1.5 (9)	**2.0 (13)**	2.5 (15)	3.0 (19)	3.5 (21)
White top-hat transformation disk size (px)	3	5	7	**9**	11	13	15
Binarization threshold	0.005	0.025	0.05	0.075	0.1	0.125	0.15

values were used by Gaddam et al. [61], however, the threshold value was varied from 0.1333 as calculated using Otsu's method, to 0.0863 and 0.1. Botero et al. [66] employed a Gaussian filter standard deviation of 2.0, filter size 7 px, white top-hat transformation disk size 2 px and automatically calculated Otsu threshold values. A subsequent study by the same author used the same values except for a Gaussian filter standard deviation of 3.0 [44]. For this study, a default value of 2.0 was chosen for the Gaussian low-pass filter standard deviation, as it lies within the previously reported range. Moreover, a range of several standard deviations was assessed to cover previously reported values (see Table 1). The respective filter sizes were chosen accordingly as the next odd integer of six times the standard deviation, i.e. filter size 13 for the standard deviation 2.0. For the structuring element of the white top-hat transformation, a disk shape was chosen. The disk is constructed around a center pixel and as such the minimum disk size is 3 px. The default size was chosen to be 9 px and a total range from the minimum disk size to a maximum value of 15 px assessed (see Table 1). The threshold value was calculated for the respective ROI using Otsu's method [62]. To assess the impact of the threshold value on the fringe metrics, a range of values was additionally tested (see Table 1).

Upon extraction of the raw fringes, a series of automated steps for qualitative cleaning was performed. First, fringes near the ROI border were removed. These could have been partially cut off during the ROI cropping, thus not representing real fringes. Secondly, a minimum fringe length threshold was imposed as fringes below this set length are likely to be artifacts. The value for this threshold varies across the literature. The range spans from values as small as the size of a single aromatic ring as used by Galvez et al. [39], to the crystallite size of 1.5 nm as used by Shim et al. [38]. For this study, a value of 0.4 nm was employed in the methodology by Yehliu et al. [40] and previously suggested by Vander Wal et al. [67]. Moreover, branched fringes can occur due to artifacts from previous image processing or graphitic defects of the sample. Such fringes were resolved by disconnection at the branch point and subsequent reconnection of the longer branches with similar orientation. Lastly, a maximum fringe tortuosity threshold was imposed. Fringes with a tortuosity greater than three were disregarded in this study, as these were assumed to stem from image processing errors rather than represent fringes in a graphitic structure.

To assess the influence of image quality and simulating differences in camera equipment, repeated images of the same particles were obtained. A total of six images for four different particles of the carbon black sample were acquired. To correct for any stage or particle drift, the images were aligned using the script StackReg for ImageJ [68]. Subsequently, the respective sections of the stacked images were averaged based on intensity.

Based on previously established optimal processing parameters, a larger number of particles were analyzed to enable a quantitative comparison. A target of 4000 fringes for each sample was chosen, slightly above previously suggested 3500 fringes or 7 particles by Zhang et al. [69]. The total fringe numbers were 4066, 4045, and 4034 for the GDI, diesel, and carbon black sample, respectively. These were extracted from 15 particles with a total ROI size of 3861 nm^2 for the GDI sample, 22 particles with total ROI size of 4026 nm^2 for the diesel sample, and 11 particles with total ROI size of 3736 nm^2 for the carbon black sample. The ROI size for each individual particle ranged from 85 nm^2 to 512 nm^2.

3. Results and discussion

Primary particles of the soot from a GDI and a diesel engine as well as carbon black were analyzed. The ROI measured 361 nm^2, 144 nm^2, and 348 nm^2, respectively. The particles are depicted in Fig. 1 with the respective regions marked as annotations and enlarged sections for better display of the nanostructure.

3.1. Gaussian low-pass filter standard deviation

The effect of changes to the standard deviation of the Gaussian low-pass filter was assessed by varying the parameter as described in Table 1. For the white top-hat transformation disk-shaped element, the default value was used throughout and the binarization threshold was calculated for each parameter case using Otsu's method. The fringe length remains mostly stable for standard deviations of 1.5 and above (see Fig. 2(a)). Slightly lower fringe lengths for standard deviations for 1.0 and even more so for 0.5. This can be particularly observed for the GDI soot and carbon black particles with sudden decreases of 38% and 41%, respectively. The diesel particle exhibits a rather linear decrease in fringe length for standard deviations greater 2.0 by 3.8–5.5% per step.

Similar to the fringe length, the fringe tortuosity does only change slightly for filter standard deviations between 1.0 and 3.5 (see Fig. 2(b)). However, instead of a sudden drop in tortuosity, a steep increase can be observed for the lowest standard deviation. This is the case for both the GDI soot and carbon black particle with increases of 72% and 61%, respectively. In contrast, the diesel soot particle exhibits a tortuosity increase of only 4.4% from the standard deviation 1.0 to 0.5. While the fringes of all three particles decrease almost continuously from the parameter cases of 1.0 to 3.5, the GDI soot particle shows a more noticeable overall increase of 17% compared to 9.6% and 5.6% for carbon black and diesel soot, respectively.

The calculated binarization threshold continuously decreases for all particles with increasing filter standard deviation (see Fig. 2(c)). For the value range of 1.0 to 3.5 this change occurs almost linearly. This is most noticeable for the carbon black particle. While the binarization value for the GDI and diesel soot particle decreases less uniformly, a linear trend is still clearly visible. In contrast to the diesel soot particle, the other two particles exhibit a much higher threshold value for the 0.5 standard deviation case.

To evaluate changes in the number of fringes, the total fringe count for the parameter cases were normalized with respect to the 2.0 default filter standard deviation point. A decrease in total fringe number with increasing standard deviation can be observed for all particles (see Fig. 2(d)). While both GDI soot and carbon black fringe counts suddenly decrease for the minimal standard deviation of 0.5, the diesel soot particle increases even further to its maximum fringe count. The largest number of fringes for the former two former particles is extracted at 1.0 filter standard deviation.

To better understand these observations, overview sections of the extracted fringes for several parameter cases are presented (see Fig. 3). Noticeably, both GDI soot and carbon black particles exhibit

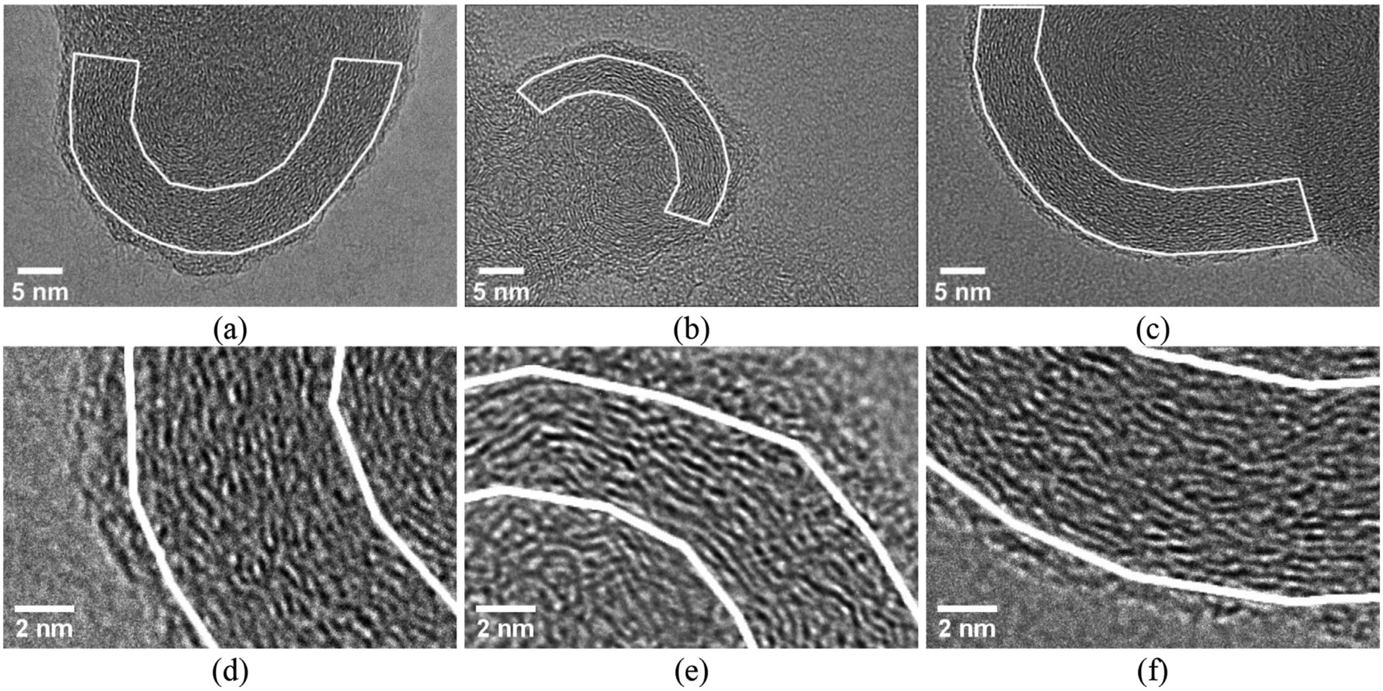

(a) (b) (c)

(d) (e) (f)

Fig. 1. HRTEM images of GDI soot (a), diesel soot (b), and carbon black (c) primary particles with the respective annotated ROI. Further, enlarged sections of these selected ROI for GDI soot (d), diesel soot (e), and carbon black (f).

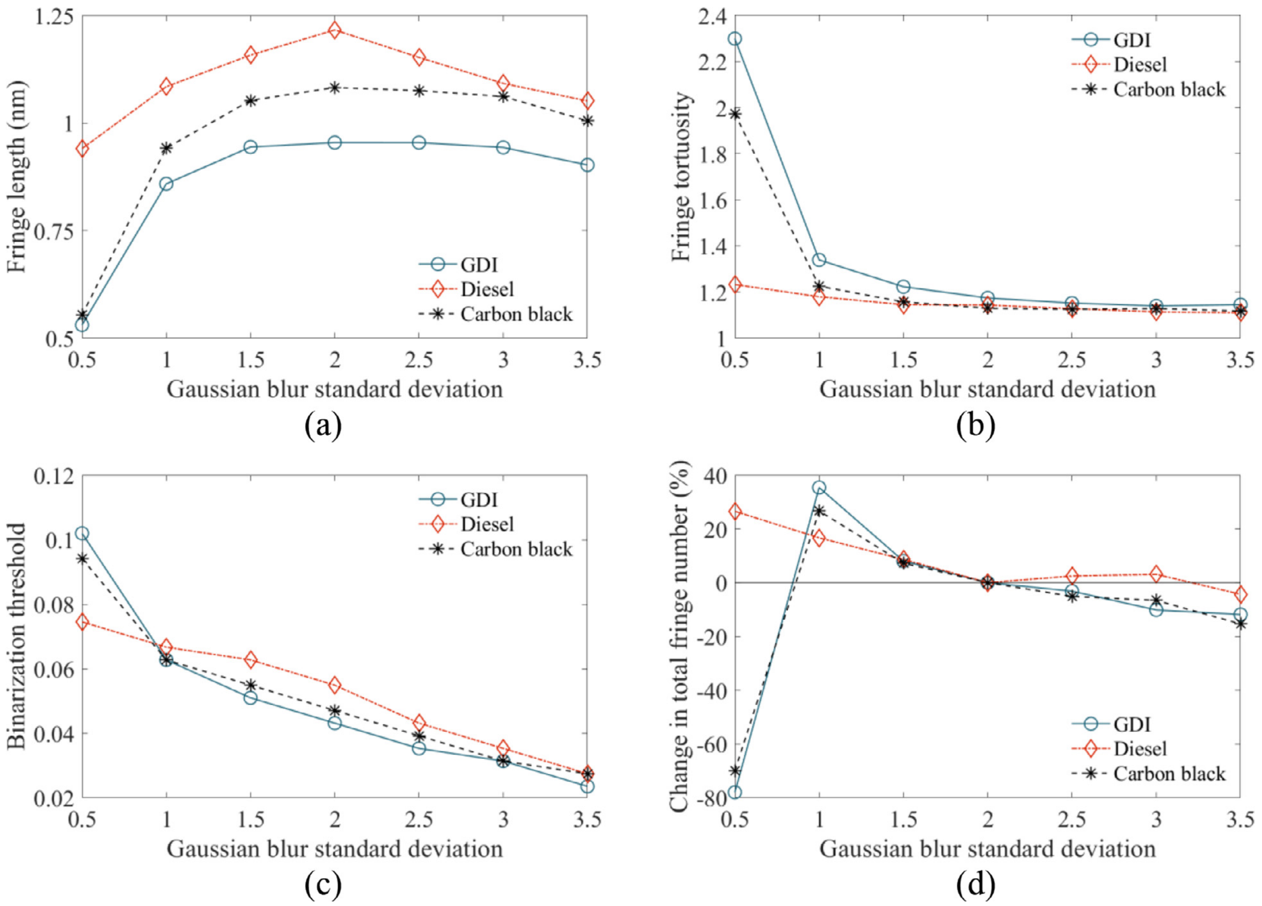

Fig. 2. Variation of fringe length (a), tortuosity (b), binarization threshold (c), and normalized total fringe number (d) with different values for the Gaussian low-pass filter standard deviation.

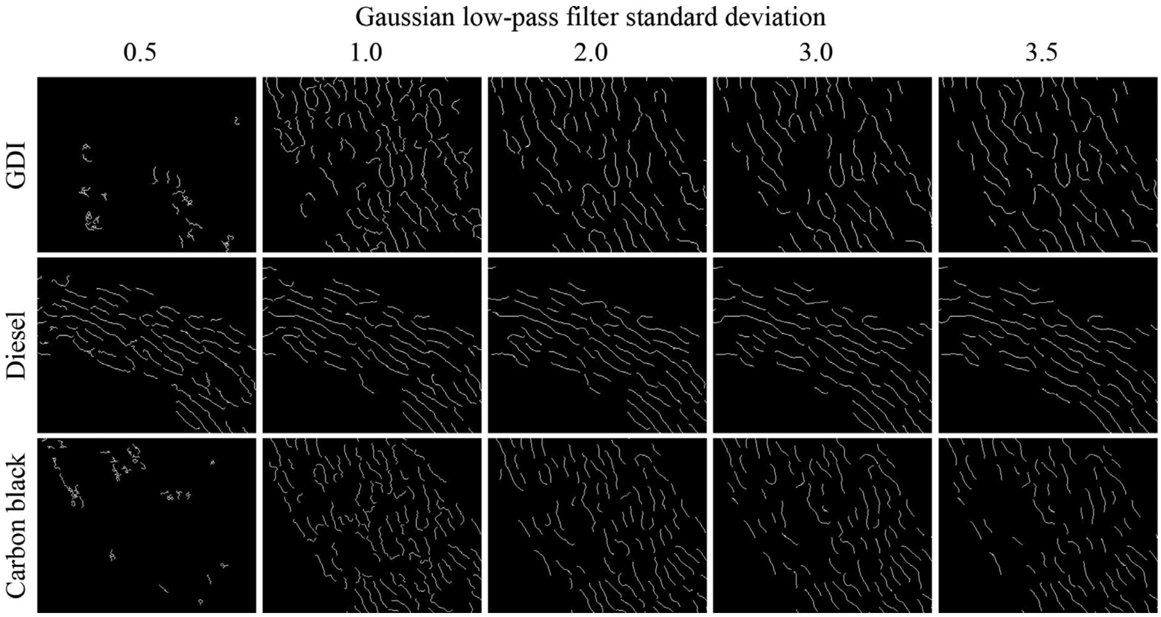

Fig. 3. Changes in fringe appearance with varying standard deviation of the Gaussian low-pass filter.

drastically fewer fringes for the 0.5 standard deviation case. The remaining fringes appear distorted, short, and twisted, rather than representing any actual graphitic carbon structure. This clearly explains the decrease in fringe length and spike in tortuosity. In contrast, the image of the diesel soot primary particle does not exhibit this behavior. All initial TEM images were taken at the same magnification and using the same settings, i.e. yielding the same spatial resolution of 0.025 nm/px. A potential cause could be the relatively small filter size of 3 px, however, this would not explain why the diesel soot particle is not affected. Thus, the difference could rather stem from the different sizes of the selected ROI; the diesel soot particle ROI is approximately 60% smaller than the ROI of the other two particles.

Aside from the lowest standard deviation, a similar appearance of the nanostructure can be observed for the three particles. Compared to the 2.0 baseline standard deviation, the density of fringes is noticeably higher for a lower 1.0 standard deviation as it could be expected with a higher total number of fringes. However, many of these fringes are less aligned to the surrounding fringes. These are more likely to stem from remaining noise due to insufficient filtering rather than representing the actual graphitic carbon nanostructure. In contrast, the density of fringes reduces with higher standard deviations. While the difference between 2.0 and 3.0 standard deviation is only minor, the highest standard deviation of 3.5 visibly appears to reduce the number and length of genuine fringes of the graphitic structure. The former two parameter values have also been found to yield similar fringe length and tortuosity, as described above. Thus, values between 2.0 and 3.0 can be deemed suitable. This is in line with values used by Botero et al. [44,66] but higher than the standard deviation used in the initial publication of Yehliu et al. [40].

3.2. White top-hat transformation disk size

The effect of the element size in the morphological processing on the fringes was assessed by performing white top-hat transformation on the images with varying disk sizes as described in Table 1. Gaussian low-pass filtering was carried out prior to the transformation using the default standard deviation of 2.0. The threshold value was calculated using Otsu's method upon completion of the transformation.

Across all three particles, a linear increase in fringe length can be observed with larger disk sizes (see Fig. 4(a)). In addition to correcting for uneven illumination, the white top-hat transformation also removes any elements that are larger than the structuring element. As such, less information is being deleted with larger disk sizes. Thus, less noise is removed, and fringes appear longer. Noticeably, the increase in fringe length is more linear and steeper for disk sizes above the default value of 9 px than for values below this point. For disk sizes smaller than the default value, both the diesel soot and the carbon black particle exhibit a local maximum in fringe length at 5 px and 7 px, respectively. In contrast, the GDI soot particle exhibits a continuously increasing fringe length with disk size, however, at a slower rate below the default disk size than above.

Similarly, the tortuosity increases more steadily for disk sizes above the default value (see Fig. 4(b)). While all particles exhibit an overall increasing trend for the tortuosity with larger disk sizes, the changes are not uniform. For both GDI and diesel soot particles a local maximum can be observed at 5 px and a larger increase in tortuosity when comparing the disk size 11 px to 13 px. For the carbon black particle, a distinctive peak in tortuosity can be observed at 7 px disk size. After a drop for the 9 px default disk size, the tortuosity increases again very linearly towards the maximum disk size.

As for the change in fringe lengths, a linear increase of the binarization threshold with the transformation disk size can be observed (see Fig. 4(c)). This can be traced back to the varying extent of information removed and residual noise. As more noise remains in the image, a higher threshold value has to be used to attain the same maximum separability of the resulting binary classes. The increase appears to occur in two phases with different rates. Below the default value of 9 px the threshold increases at a rate of 0.007 per px, while above this value the rate is more than twice as high with 0.017 per px.

In contrast to the aforementioned characteristics, the total number of fringes exhibits an overall decreasing trend with increasing disk size (see Fig. 4(d)). However, the highest number of fringes can be extracted for the diesel soot and carbon black particle with a disk size of 7 px. For both particles, the total fringe number decreases not just towards larger disk sizes but also for the smallest 3 px disk. The GDI soot particle exhibits the highest

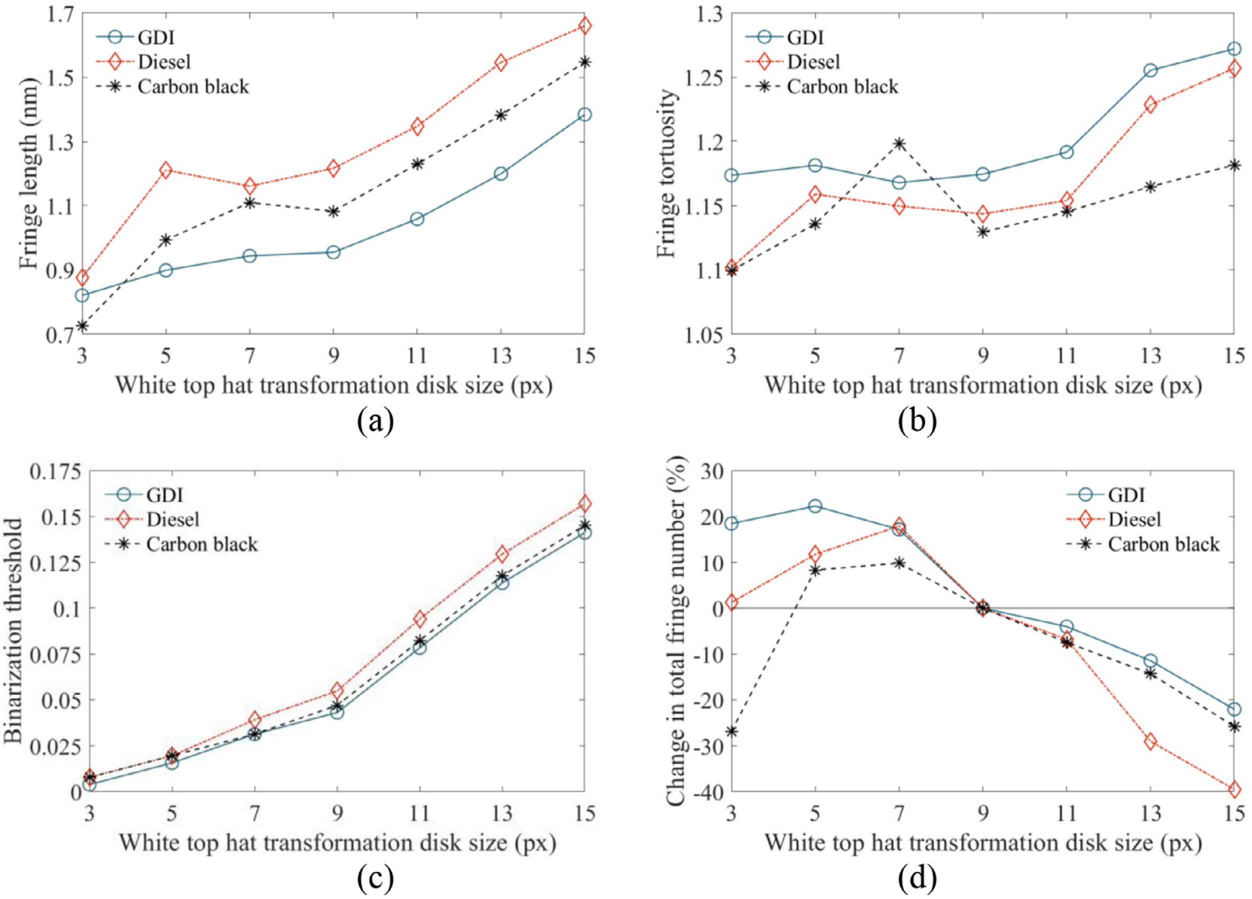

Fig. 4. Variation of fringe length (a), tortuosity (b), binarization threshold (c), and normalized total fringe number (d) with different values for the white top-hat transformation disk size.

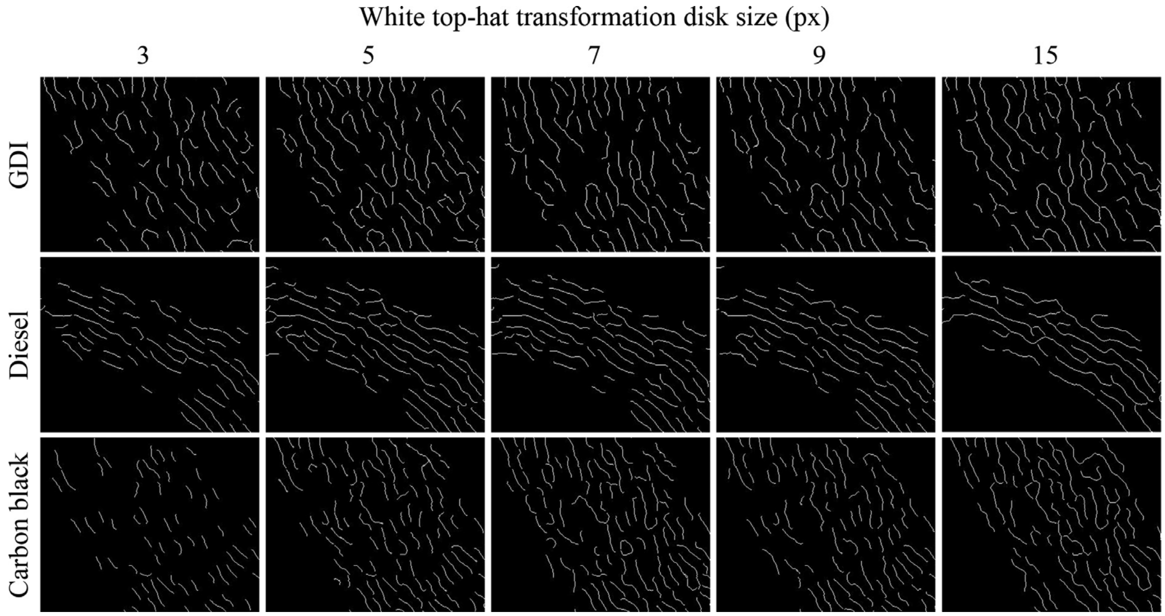

Fig. 5. Changes in fringe appearance with varying disk size of the white top-hat transformation.

number of fringes at 5 px. While GDI soot and carbon black particle fringe count decrease at a similar rate towards larger disk sizes, the number of fringes from the diesel soot particle decreases more rapidly.

To better understand the changes in fringe characteristics, overview sections of the extracted fringes for several parameter cases are provided in Fig. 5. With lower disk sizes the fringes shrink noticeably as meaningful information is removed alongside with noise. At the same time, the total number of fringes increases with the exception of the carbon black particle at the minimum disk size parameter case. This can be attributed to longer fringes being split into multiple sections. The obtained set of fringes

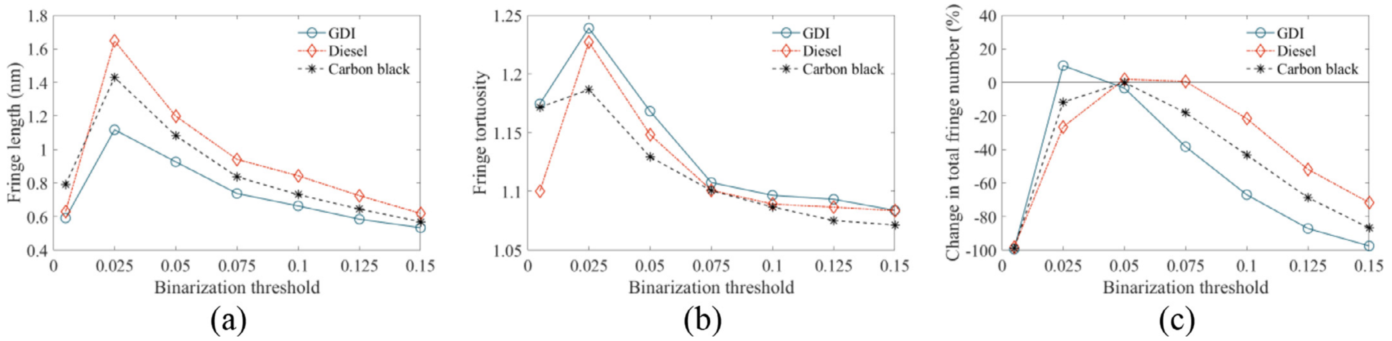

Fig. 6. Variation of fringe length (a), tortuosity (b), and total fringe number (c) with different values for the binarization threshold.

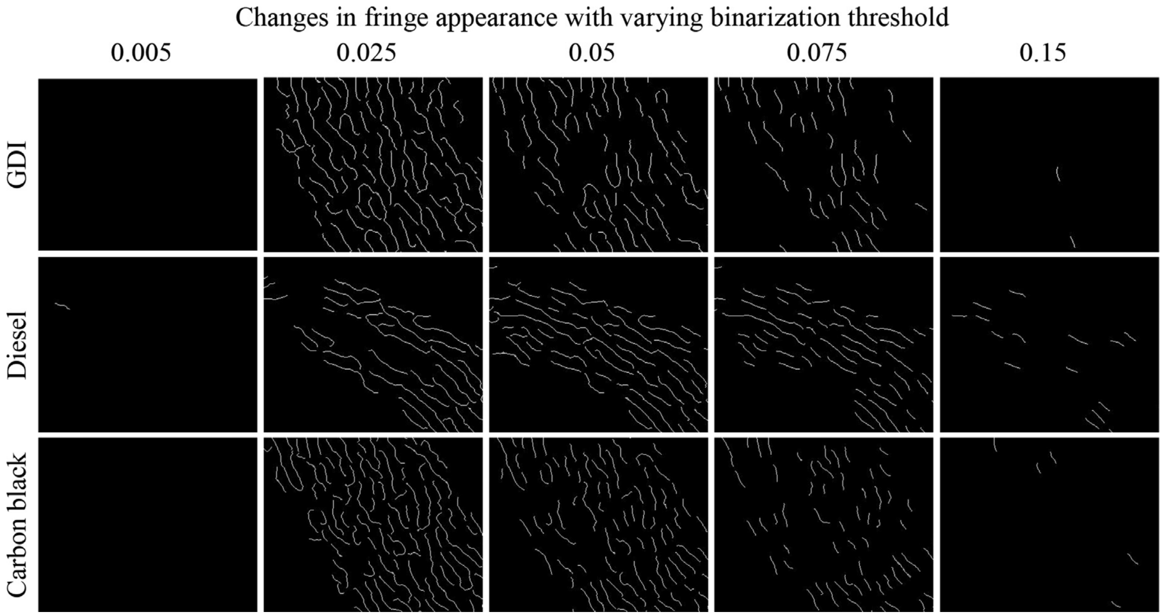

Fig. 7. Changes in fringe appearance with varying binarization threshold.

exhibits larger spaces and voids and is thus less representative of the actual nanostructure. For larger disk sizes, fringes appear to grow and merge as less information is removed. This poses the opposite problem, of fringes growing being lengthened due to artifacts becoming part of the fringes. Therewith, the nanostructure is again not accurately represented in such cases. Disk sizes between 5 px and 9 px appear to yield the most realistic representation of the graphitic structure. The average variation in fringe length and tortuosity between these disk sizes is 4.9% and 2.4%, respectively. Due to the higher total number of fringes, the disk sizes of 5 px and 7 px are here recommended for future studies.

3.3. Binarization threshold

As observed in the sections above, the image processing parameters Gaussian low-pass filter standard deviation and white top-hat transformation disk size can greatly influence the threshold as calculated by Otsu's method. Moreover, information and quality of the fringe analysis depend on the residual noise as well as image properties, i.e. brightness and contrast. To assess the impact of the threshold value itself, a series of binarization threshold values was employed as described in Table 1. For the Gaussian low-pass filter and the white top hat transformation disk size the default values were used, i.e. 2.0 and 9 px, respectively. The Otsu threshold values using these parameters are 0.043, 0.055, and 0.047 for the GDI soot, Diesel soot, and carbon black particle, respectively.

For all three particles, the fringe length is the highest at the binarization threshold of 0.025 and appears to decay exponentially for larger threshold value (see Fig. 6(a)). However, for the smaller threshold of 0.005, the fringe length decreases across all particles. Similar observations can be made for the fringe tortuosity (see Fig. 6(b)). The highest tortuosity of the fringes can be observed at 0.025 and decrease from there for both higher and lower threshold values. However, the decrease towards higher threshold values is less exponential but exhibits rather two phases. While the tortuosity decreases rapidly up till the threshold value 0.075, the reduction beyond this parameter case is slower.

To evaluate the effect on the number of fringes, the respective fringe counts were normalized with respect to the number of fringes as for the parameter case using the Otsu threshold. The fringe counts appear to be normally distributed with the maximum around the Otsu threshold and positively skewed towards larger threshold values (see Fig. 6(c)). While a lower threshold of 0.025 yields a higher number of fringes for the GDI soot particle, the Otsu threshold generally extracts the most fringes. Across all particles, the number of fringes rapidly drops to zero for the lowest threshold value. Towards larger threshold values the decrease is slower.

The changes also become noticeable when looking at overview sections of the extracted fringes (see Fig. 7). For both the highest and lowest threshold value, almost no fringes were extracted. The threshold closest to the individual Otsu threshold values is 0.05. For the GDI soot and carbon black particle, clear changes

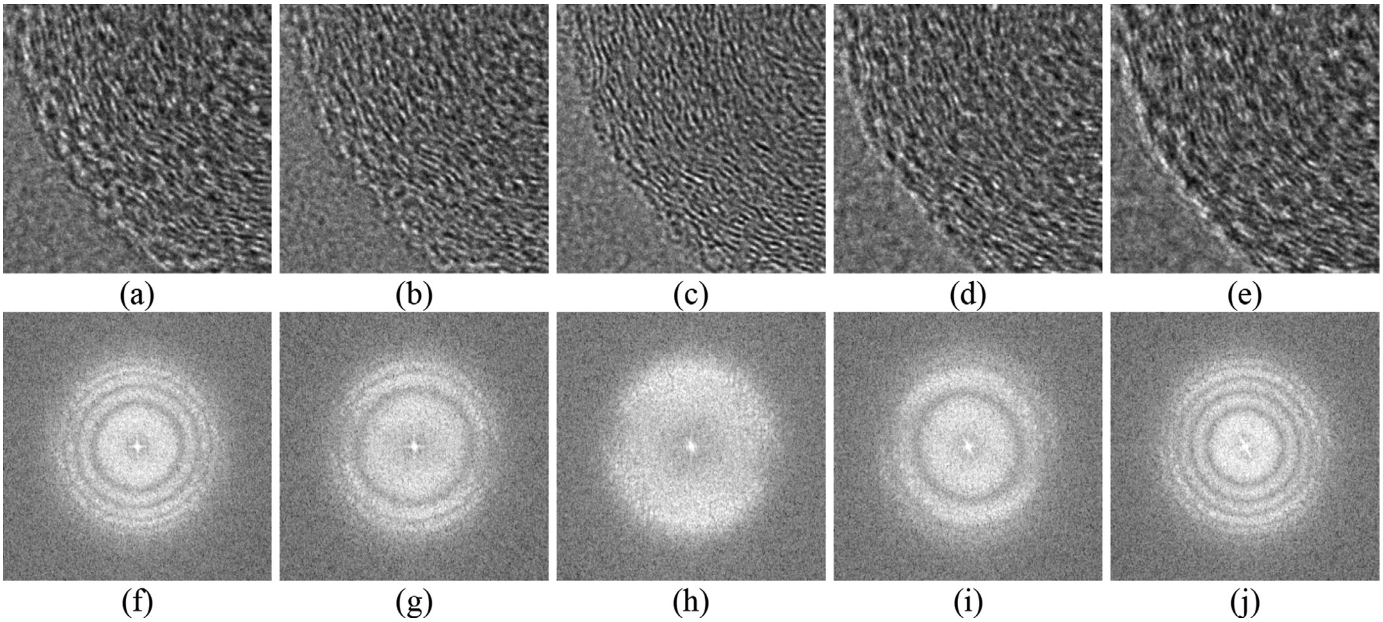

Fig. 8. TEM images of particle P2 of the carbon black sample in different focus points and corresponding fast Fourier transformations: under-focused by 90 nm (a, f), under-focused by 45 nm (b, g), neutral-focused (c, h), over-focused by 45 nm (d, i), over-focused by 90 nm (e, j).

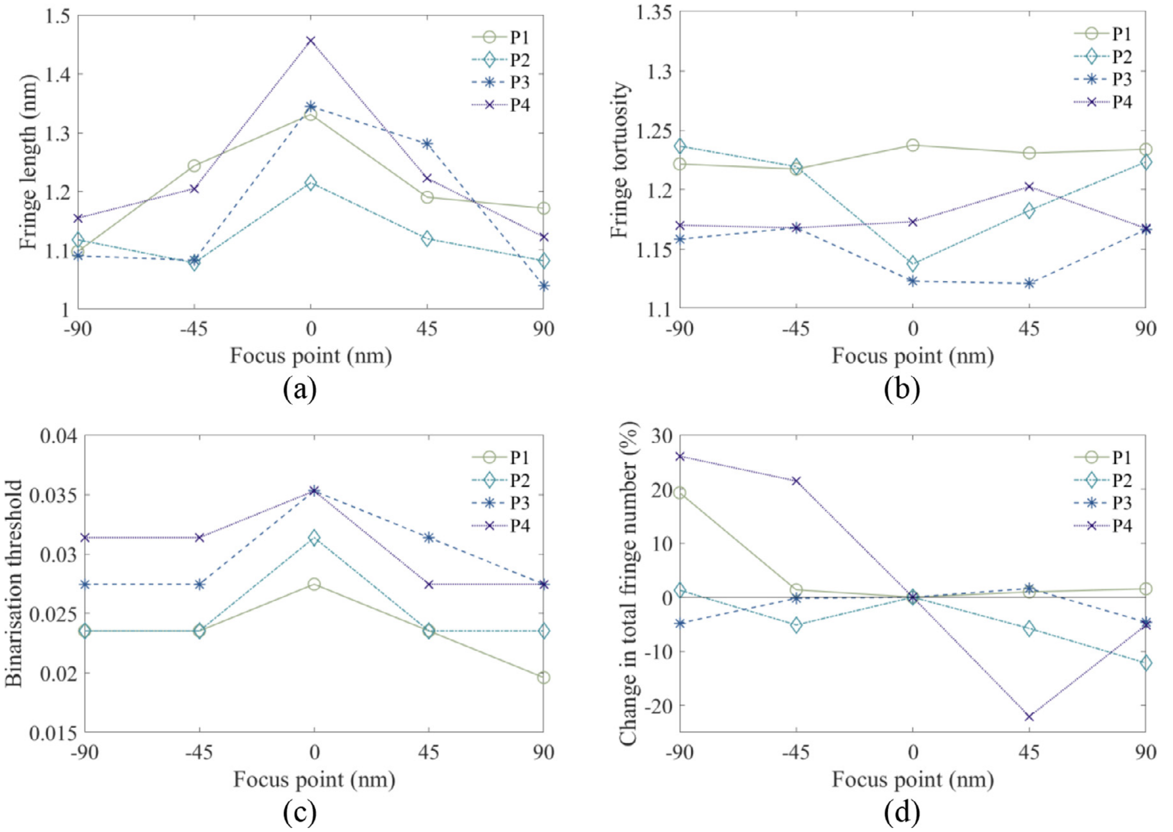

Fig. 9. Variation of fringe length (a), tortuosity (b), binarization threshold (c), and normalized total fringe number (d) with different TEM focus points.

can be observed if the fringes at 0.05 threshold are compared to the fringes of the adjacent threshold values. For the 0.025 threshold value, the fringe network appears denser, i.e. the fringes are longer and do not just follow the parallel graphitic layers but also extend across the interlayer spaces. In contrast, for the 0.075 threshold value, the fringes are noticeably shorter and lower in number. The diesel soot particle shows similar tendencies, however, at a slower rate indicating a wider spread distribution.

The specific values for the observed fringe length and tortuosity values would change for different settings of Gaussian low-pass filter size and white top-hat transformation disk size. However, the analysis here is made relative to the respective Otsu's threshold and the subsequent deviation from it. Any changes due to parameter influence would shift the values but not the observable trend. For future studies, the use of the threshold value as calculated by Otsu's method is here recommended. This method yields among the highest number of fringes and no beneficial reason for any deviation was observed.

The findings presented here contradict earlier results by Gaddam et al. [61]. In their study, no significant variation of the fringe metrics with varying threshold values was observed. The maximum difference in fringe length was 0.05 nm. The change in fringe length here from the parameter case closest to the respective Otsu threshold values (0.05) to the neighboring cases ranges from 0.19 nm to 0.45 nm. While the change in metrics decreases to 0.05–0.1 nm per parameter step towards larger threshold values, a clear trend as well as differences between parameter cases is still notable.

3.4. TEM focus point

To assess the influence of the focus of the TEM on the observed fringes, four particles of the carbon black sample were used (labeled as P1, P2, P3, and P4). Five images with different focus points were acquired for each particle. The baseline focus point at which the particle is deemed in focus was set by the TEM operator visually and aided by the fast Fourier transformation (FFT) of the particle region. When the particle region is in focus, the respective FFT shows only one bright circle. With increasing defocus additional dark and bright rings become apparent (see Fig. 8). From the central neutral focus point, the focus was changed by a total of 90 nm in two equal steps each way.

The longest fringes can be obtained for each particle when the microscope is in the central focus point (see Fig. 9(a)). When compared in this point, the fringe length varies among the particles of the same sample by up to 0.25 nm, as given by the difference between the particles P2 and P4. This intra-sample variation, i.e. particle to particle differences, has also previously been observed by Zhang et al. [69]. By under- and over-focusing the fringe length can change by as little as 0.14 nm and up to 0.33 nm for particles P2 and P4, respectively. As the variations due to changes in the focus point are larger than the intra-sample variation, there is a case for carefully choosing the focus. While the effective variation of focus selection within sessions or even between TEM operators might be smaller than the stated values, these findings highlight the importance of this parameter for fringe lengths.

In contrast, no obvious trends can be observed in terms of tortuosity (see Fig. 9(b)). For both particles P1 and P4, the values remain relatively constant. Particle P2 shows increases for both under- and over-focusing as compared to the neutral focus point. However, the changes remain on a similar level as the difference across the individual particles themselves. P3 also exhibits some changes of tortuosity with varying focus points, however, these changes again do not follow any apparent trend. Similar observations can be made for the change in the number of fringes.

To assess any variations, the total number of fringes is normalized with respect to the neutral focus point. Fringe counts for particle P1 remain relatively stable around the baseline, except for the furthest under-focused point at which the number increases suddenly by 19.3% (see Fig. 9(d)). Smaller differences can be observed for P2 and P3 with up to +1.6% and −12.2%, respectively. Total fringe numbers for both slightly decrease towards the over-focused side but do not show a clear tendency when under-focusing. Particle P4 shows the greatest changes in total fringe number with +26% and −22% for under- and over-focusing, respectively. However, no clear trend in the change of total fringe number can be observed with changes in the focus across the particles.

The binarization threshold as determined by Otsu's method shows a clear peak across all particles for the center focus point (see Fig. 9(c)). For the two under-focused points, the threshold drops to a lower value for all particles regardless of the degree of under-focusing. On the over-focused side, the threshold values for P2 and P4 exhibit a similar pattern. While the respective values for P1 and P3 also decrease, this reduction is more pronounced with a higher degree of defocus. This pattern appears to be similar to the observed changes in fringe length. Contrary to the inverse correlation mentioned above, the fringe length decreases despite the reduction in the binarization threshold. The changes in the fringes are therefore not an artifact of altered contrast, but rather directly affected by the distorted image of the nanostructure. Previously, Wan et al. [63] suggested based on simulated images that the TEM focus could have a considerable influence on the fringe metrics. The experimental approach in this study provides the necessary evidence to confirm this hypothesis. Consequently, the uniform and consistent setting of the focus point across samples and particles is paramount for meaningful results. As of today, this decision heavily relies on the TEM operator. Previously, Kondo et al. [64] observed that the operator's experience can greatly affect the selection of characteristic regions of a given agglomerate. It is here suggested that this could also apply to the focus point. The point of focus is commonly selected by the visual appearance and aided by live Fourier transformations of the respective particle region. However, the implementation of a tool for automatic calculation of the Otsu binarization threshold could quantitatively aid this process in the future.

3.5. Image quality and noise

As outlined above, several aspects of image quality such as uneven image illumination or TEM focus can influence the fringe analysis results. Likewise, metrics such as spatial resolution and signal-to-noise ratio can play a role. Both are affected by the standard of the available camera as well as parameters such as exposure times. For this study, a Gatan Orius CCD camera was used, yielding a spatial resolution of 0.025 nm per pixel at 500,000× magnification. Images were acquired with an exposure time of one second. Longer exposure times give better signal-to-noise ratios but can prove particularly challenging due to stage and sample drift. Hence, a series of six images was acquired for each of the four particles, to assess the effect of image quality. To account for any drift between images, the images were aligned using the script StackReg for ImageJ [68]. The images were progressively stacked and intensity averaged.

Some noticeable fluctuation can be observed for the fringe lengths to different extents across the particles (see Fig. 10(a)). While the variation between stacks of different images is only up to 3% for P1, P3 exhibits differences of up to 9%. However, the standard deviation of the values across the averaged image stacks is similar for all particles with 3–4%. Despite the variations in the measurements, no apparent trend in the data can be identified.

Similar observations can be made for the fringe tortuosity (see Fig. 10(b)). However, the variation between image stacks is relatively lower with up to 3% for P1 and 2% for the remaining particles. Likewise, the standard deviation across the averaged images is 2% for P1 and 1% for the other particles. As for the fringe length, there is no evident trend of the tortuosity across the averaged images.

The Otsu threshold does not change for any of the particles with the number of averaged images (see Fig. 10(c)). In contrast, the total fringe number clearly decreases with an increasing number of averaged images (see Fig. 10(d)). For particle P1 the number of fringes decreases almost linearly by around 2% after an initial drop of 7% for the second image added to the averaged stack. The fringe count for P2 remains relatively constant until 3 images, after which the number of fringes creases by 5%. Despite slightly in-

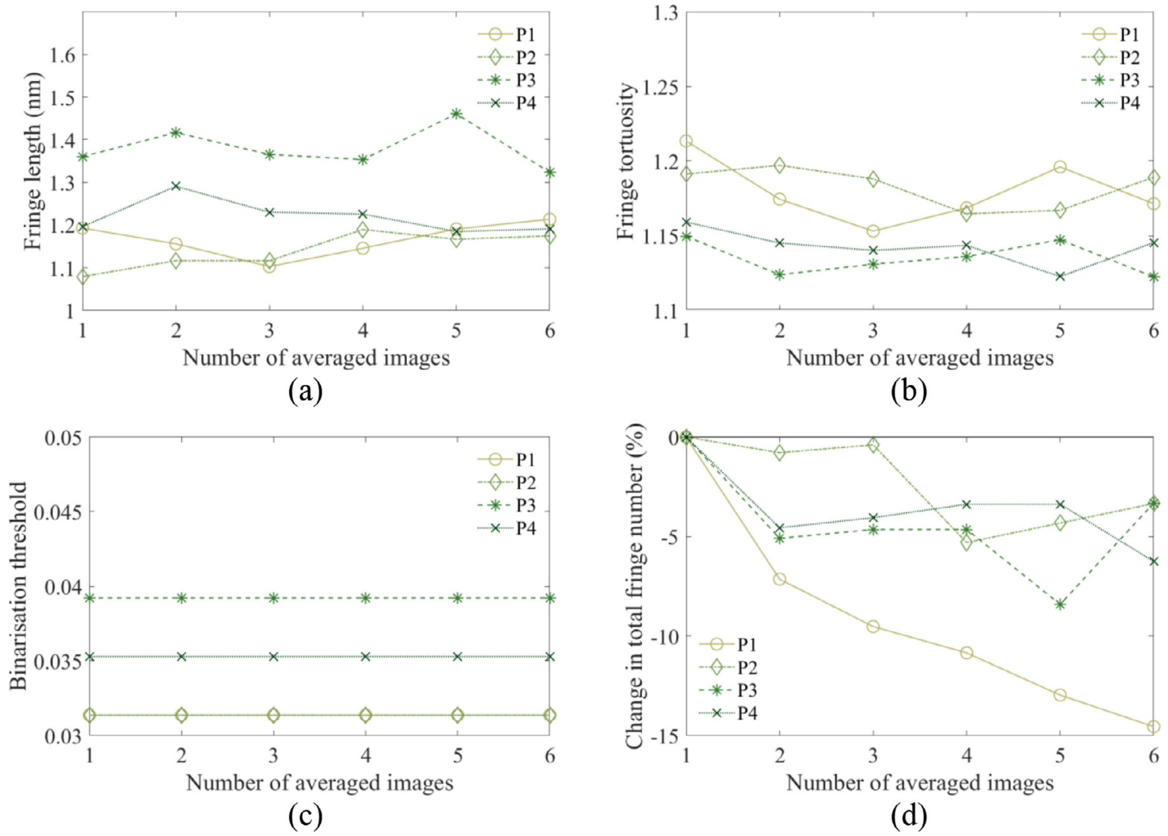

Fig. 10. Variation of fringe length (a), tortuosity (b), binarization threshold (c), and normalized total fringe number (d) with the number of images averaged.

creasing afterward by 1%, the number remains at a lower level. P3 and P4 also decrease with the second image added to the averaged stack as P1, however, only by 4–5%. Contrary to P1, the total fringe number does not decrease further linearly but remains on a similar level despite some fluctuations. It should be noted that the observed changes of total fringe numbers for averaged images are on a lower scale as compared to the previous processing parameters as well as the TEM focus points. As the two fringe measurements do not show any noticeable trend, it is suggested that the used camera is either simply sufficient for this purpose or the contribution of this aspect is rather minor.

3.6. *Region of interest size*

The purpose of any fringe analysis is the characterization and ultimately comparison of different samples. Qualitative reliability has been established above by determining the appropriate values for the used processing filters as well as investigating the influence of the TEM focus point and image quality. To allow for a meaningful comparison of samples, the requirements for quantitative reliability have to be established. This can be achieved by means of a sufficient number of analyzed fringes for statistical significance. Zhang et al. [69] had suggested a threshold of seven primary particles with a total of 3500 fringes for reliable fringe metrics. Here, a slightly higher threshold of 4000 fringes was implemented. A total fringe number of 4066, 4045, and 4034 were obtained for the GDI, diesel, and carbon black sample, respectively. These were extracted from 15 particles with a total ROI size of 3861 nm^2 for the GDI sample, 22 particles with total ROI size of 4026 nm^2 for the diesel sample, and 11 particles with total ROI size of 3736 nm^2 for the carbon black sample. The ROI size for each individual particle ranged from 85 nm^2 to 512 nm^2. To assess any potential influence of this aspect, total fringe number, fringe length, and fringe tortuosity were plotted against ROI size (see Fig. 11). Moreover, linear regression models (LRM) were fitted for each collective data set.

The total fringe number shows a strong correlation with the ROI size as the model fits the data well with a coefficient of determination $R^2 = 0.99$. The associated $p = 1 \times 10^{-46}$ indicates strong statistical significance. In contrast, the linear models for fringe length and tortuosity cannot explain the observed variation with $R^2 = 3 \times 10^{-4}$ and $R^2 = 7 \times 10^{-4}$, respectively. Based on the respective p-values of $p = 0.91$ and $p = 0.86$, no significant linear correlation between the fringe metrics and the ROI size can be observed.

If the ideal processing parameters would change for a given nanostructure image, this would alter the number of fringes and the fringe metrics itself as observed in the subchapters 3.1–3.3 above. Such changes would be expected to manifest in the form of a non-linear trend in the total fringe number as well as linear trends in the fringe metrics over different ROI sizes. Neither could be observed here. Thus, the size of the ROI only affects the total number of fringes due to a different size of particle nanostructure covered.

3.7. *Total fringe number and sample comparison*

Despite the fact that the ROI size does not influence the fringe metrics, the total number of extracted fringes can play a role. This aspect was to date only addressed as part of a study by Zhang et al. [69]. Fringe analysis was performed on several primary particles and the cumulative moving average (CMA) of the fringe metrics subsequently assessed. It was observed that the 95% confidence intervals decreased with higher numbers of processed images of primary particles, i.e. increased quantitative reliability.

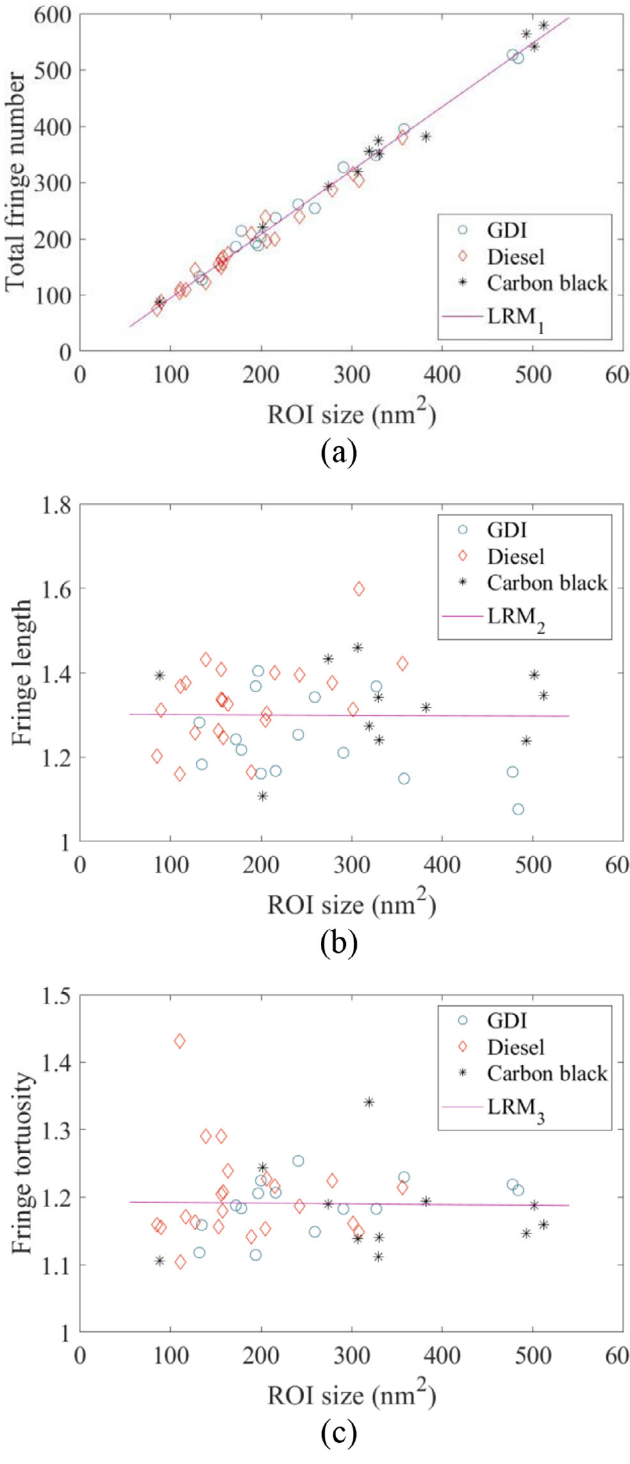

Fig. 11. Total fringe number (a), fringe length (b), and fringe tortuosity (c) of the respective region of interest (ROI) with fitted linear regression model (LRM$_1$: R^2=0.99, $p=1 \times 10^{-46}$. LRM$_2$: R^2=3 × 10^{-4}, $p=0.91$. LRM$_3$: R^2=7 × 10^{-4}, $p=0.86$).

Both averaged fringe length and tortuosity converged for more than seven primary particles or 3500 fringes. However, the number of fringes that was extracted from each particle was not further specified. As this number can vary noticeably, as described above, the following analysis is based on the total fringe number. For the processing, a Gaussian low-pass filter standard deviation of 2.0, white top-hat transformation disk size of 7 px, and the Otsu's threshold value for the binarization were used. The CMA fringe length and tortuosity is plotted over the cumulative total fringe number in Fig. 12. To assess the statistical significance, 95% confidence intervals were calculated every 500 fringes.

The highest fluctuation can be observed below 500 fringes with confidence intervals of the three samples clearly overlapping. Some further changes in mean values occur between 500 and 2000 fringes. In terms of fringe length, GDI soot sample remains stable beyond 2000 fringes, whereas both the diesel soot and carbon black sample drift before crossing at 3000 fringes and then stabilizing. A clear difference between the GDI soot and the two other samples can be observed, of 0.14 nm and 0.1 nm to the mean values of diesel soot and carbon black sample, respectively, at 4000 fringes. The confidence intervals of all samples at this data point are just under ± 0.3 nm. Despite the difference and drifts in mean values between diesel soot and carbon black, the confidence intervals overlap consistently, being almost identical at 3000 fringes. Thus, no statistically significant difference between the fringe lengths of these two samples can be identified with this analysis. Regarding fringe tortuosity, the appearance of the CMA plots is different as drifts continue longer. A slight positive drift can be observed for the GDI soot sample and even stronger for the carbon black sample. Both values stabilize around 3000 fringes. In contrast, the CMA tortuosity for the diesel soot sample does not converge but rather shows a subtle negative trend with an increasing number of fringes. Similar tortuosity values with overlapping error bars are observed for the GDI and diesel soot samples up to 3000 fringes. Above this point, the tortuosity is lower for the diesel soot sample. The carbon black particles exhibit a lower tortuosity CMA throughout the total fringe number range. The mean values of the GDI and diesel soot samples are higher by 0.021 and 0.01, respectively. The confidence intervals range between 0.0046 (carbon black) and 0.0052 (GDI soot) and despite being close, they do not overlap across the samples.

Absolute numerical comparisons are problematic due to often insufficiently reported processing parameters. However, ranged and differences can be compared. Li et al. [17] observed changes to the fringe length of up to 0.06 nm (1.16–1.2 nm) and tortuosity of 0.07 (1.13–1.2) with different fuel injection modes in a diesel engine. For various injection timings, Xu et al. [70] found even greater differences in nanostructure of up to 0.28 nm (1.12–1.4 nm) in fringe length and 0.13 (1.12–1.25) in tortuosity. For a GDI engine, Wu et al. [41] saw for different air–fuel ratios changes in the nanostructure of 0.08 nm (0.83–0.91 nm) in length and 0.05 (1.44–1.49) in tortuosity of fringes. Similarly, Gaddam and Vander Wal [26] observed changes for various GDI engine conditions of up to 0.1 nm (0.72–0.82 nm) in length and 0.03 (1.18–1.21) in tortuosity. Previous investigations that included also Raman spectroscopy indicated a higher degree of order for carbon black over diesel soot, with GDI soot showing the lowest degree of order [32]. GDI soot appears here as well to be of lower structural order compared to carbon black. The results for diesel soot diverge. The fringe length is similar to carbon black but the tortuosity is different. Meanwhile, the gaps between samples observed here are on a comparable scale as for samples with different nanostructures analyzed in other works. The additionally reported confidence intervals in this study to allow for better appraisal of the results in terms of significance. Overall, the differences between the three types of soot can likely affect a series of properties, such as oxidative reactivity [41], interaction with lubricating oil [71] or wear behavior [72] in engine applications.

In terms of the total fringe number required for reliable data, 3000 fringes appear to be a lower limit for convergence of the CMA. Here it is recommended that 4000 fringes should be used as threshold value for analysis to ensure a stabilized window of roughly 1000 fringes prior to the data point used.

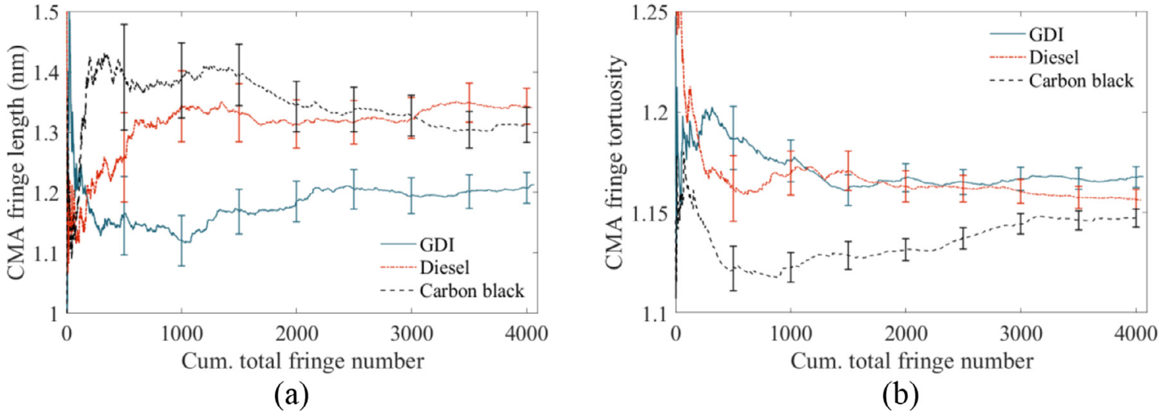

Fig. 12. Cumulative moving average (CMA) of fringe length (a) and tortuosity (b) for the cumulative total fringe number. The error bars are indicative of 95% confidence intervals.

4. Conclusions

Soot particles from different emission sources were used to assess the influence of three image processing parameters of an established fringe analysis methodology:

- The effect of the Gaussian low-pass filter standard deviation is minor for a range of values. However, noticeable changes in the structure of extracted fringes occur for values of 1.0 and below as well as larger 3.0. Based on the findings, standard deviations between 2.0 and 3.0 are recommended.
- A linear correlation between the white top-hat transformation disk size and fringe length, tortuosity, and Otsu threshold was observed. Moreover, an inverse correlation between the disk size and the total number of fringes was found. For a realistic representation of the nanostructure and optimized fringe numbers, the disk sizes 5 px and 7 px are here recommended.
- The use of individually calculated Otsu's threshold values generally yields the highest number of fringes. For larger threshold values, the total fringe number as well as both fringe length and tortuosity decay exponentially. Similarly, for values considerably smaller, i.e. close to 0, almost no fringes could be extracted. For best results and good repeatability, the use of the Otsu threshold without alterations is advised.

These parameters were determined for a spatial resolution of 0.025 nm/px at a magnification of 500,000×. As both Gaussian low-pass filter standard deviation and white top-hat transformation disk size are dependent on spatial resolution, similar investigations as in this study would need to be carried out if other magnifications were to be employed.

Moreover, two aspects of the TEM operation and their implications for the extracted fringes were considered:

- Deviating from the selected TEM focus point by under- and over-focusing resulted in distinctive drops in both fringe length and Otsu threshold. Despite some variations, no noticeable trends could be observed for the fringe tortuosity and total fringe number. However, to obtain reliable results, consistent focusing with the help of fast Fourier transformations is necessary across particles and samples.
- The effect of extended exposures and signal-to-noise ratio was found to be minor beyond the image acquisition equipment used. While the number of fringes decreased with multiple intensity-averaged images, the fringe length and tortuosity metrics did not show a trend in either direction.

Further, the quantitative reliability of the method was assessed:

- The size of the region of interest correlated linearly with the total number of extracted fringes ($R^2 = 0.99$, $p = 1 \times 10^{-46}$). However, the fringe metrics were not influenced by the size, as assessed by linear regression models for both fringe length ($R^2 = 3 \times 10^{-4}$, $p = 0.91$) and tortuosity ($R^2 = 7 \times 10^{-4}$, $p = 0.86$).
- The highest fluctuations in the cumulative moving average of both fringe length and tortuosity can be observed below a total number of 500 fringes, with further jumps up to 2000 fringes. The fringe metrics mostly converge when reaching 3000 fringes. Here it is recommended that 4000 fringes should be used as a threshold to ensure a stabilized window of roughly 1000 fringes prior to the data point used.

Lastly, the three different soot types were compared:

- The GDI soot sample exhibited a distinctively the lowest fringe length by more than 0.1 nm. The numerical difference of 0.4 nm between the diesel soot and carbon black fringe lengths falls within the respective confidence intervals. Thus, no statistically significant difference can be noted for the latter two samples.
- In terms of fringe tortuosity, the largest cumulative moving average was found for the GDI soot sample. The tortuosity of diesel soot and carbon black sample was found to be lower by 0.01 and 0.021, respectively. Despite the fact that the confidence intervals were close to each other, they did not overlap.
- GDI soot sample most distinctively different from the other two samples. While diesel soot sample shares some similarity with the carbon black, differences in terms of fringe tortuosity can be appreciated.

Declaration of Competing Interest

The authors declare that they have no known competing financial interests or personal relationships that could have appeared to influence the work reported in this paper.

Acknowledgments

This work was supported by the Engineering and Physical Sciences Research Council through the scholarship provided by EPSRC Thematic Programme in Low-Dimensional Materials and Interfaces for Sebastian Pfau [grant number EP/N50970X/1]. The authors thank the Nanoscale and Microscale Research Centre (nmRC) for providing access to instrumentation. The authors also thank Kayleigh Fung for the electron dose camera calibrations.

References

[1] D.M. Broday, R. Rosenzweig, Deposition of fractal-like soot aggregates in the human respiratory tract, J. Aerosol Sci. 42 (6) (2011) 372–386, doi:10.1016/j.jaerosci.2011.03.001.

[2] G. Oberdörster, R.M. Celein, J. Ferin, B. Weiss, Association of particulate air pollution and acute mortality: involvement of ultrafine particles? Inhal. Toxicol. 7 (1) (1995) 111–124, doi:10.3109/08958379509014275.

[3] X. Mari, J. Lefèvre, J. Torréton, Y. Bettarel, O. Pringault, E. Rochelle-Newall, et al., Effects of soot deposition on particle dynamics and microbial processes in marine surface waters, Glob. Biogeochem. Cycles. 28 (7) (2014) 662–678, doi:10.1002/2014GB004878.

[4] T.C. Bond, S.J. Doherty, D.W. Fahey, P.M. Forster, T. Berntsen, B.J. DeAngelo, et al., Bounding the role of black carbon in the climate system: a scientific assessment, J. Geophys. Res. Atmos. 118 (11) (2013) 5380–5552, doi:10.1002/jgrd.50171.

[5] D. Shindell, J.C.I. Kuylenstierna, E. Vignati, R. van Dingenen, M. Amann, Z. Klimont, et al., Simultaneously mitigating near-term climate change and improving human health and food security, Science 335 (6065) (2012) 183–189, doi:10.1126/science.1210026.

[6] J.B. Heywood, Internal Combustion Engine Fundamentals, McGraw-Hill, New York, 1988.

[7] H. Bockhorn (Ed.), A short introduction to the problem – structure of the following parts, in: Soot Formation in Combustion: Mechanisms and Models, Springer, Berlin, Heidelberg (1994) 3–7, doi:10.1007/978-3-642-85167-4_1.

[8] H. Richter, J.B. Howard, Formation of polycyclic aromatic hydrocarbons and their growth to soot – a review of chemical reaction pathways, 2000. doi:10.1016/S0360-1285(00)00009-5.

[9] Q. Tang, M. Wang, X. You, Effects of fuel structure on structural characteristics of soot aggregates, Combust. Flame 199 (2019) 301–308, doi:10.1016/j.combustflame.2018.10.033.

[10] Y. Araki, K. Takahashi, K. Kaga, Y. Saito, Y. Matsushita, H. Aoki, et al., Influence of aliphatic side chains of aromatic hydrocarbons on soot formation: experimental and numerical investigation, Combust. Flame 194 (2018) 195–205, doi:10.1016/j.combustflame.2018.04.034.

[11] M.M. Maricq, Soot formation in ethanol/gasoline fuel blend diffusion flames, Combust. Flame 159 (1) (2012) 170–180, doi:10.1016/j.combustflame.2011.07.010.

[12] A. D'Anna, M. Alfè, B. Apicella, A. Tregrossi, A. Ciajolo, Effect of fuel/air ratio and aromaticity on sooting behavior of premixed heptane flames, Energy Fuels 21 (5) (2007) 2655–2662, doi:10.1021/ef070159y.

[13] A. D'Anna, A. Ciajolo, M. Alfè, B. Apicella, A. Tregrossi, Effect of fuel/air ratio and aromaticity on the molecular weight distribution of soot in premixed n-heptane flames, Proc. Combust. Inst. 32 (1) (2009) 803–810, doi:10.1016/j.proci.2008.06.198.

[14] G.D.J. Guerrero Peña, A. Raj, S. Stephen, T. Anjana, Y.A.S. Hammid, J.L. Brito, et al., Physicochemical properties of soot generated from toluene diffusion flames: effects of fuel flow rate, Combust. Flame 178 (2017) 286–296, doi:10.1016/j.combustflame.2017.01.009.

[15] G.D.J. Guerrero Peña, R.K. Rahman, A. Raj, S. Stephen, T. Anjana, J.L. Brito, Effect of fuel flow rate on the characteristics of soot generated from unsubstituted and disubstituted aromatic hydrocarbon flames: experimental and numerical study, Combust. Flame 190 (2018) 224–239, doi:10.1016/j.combustflame.2017.12.010.

[16] C. Wang, H. Xu, J.M. Herreros, J. Wang, R. Cracknell, Impact of fuel and injection system on particle emissions from a GDI engine, Appl. Energy 132 (2014) 178–191, doi:10.1016/j.apenergy.2014.06.012.

[17] X. Li, C. Guan, Y. Luo, Z. Huang, Effect of multiple-injection strategies on diesel engine exhaust particle size and nanostructure, J. Aerosol Sci. 89 (2015) 69–76, doi:10.1016/j.jaerosci.2015.07.008.

[18] X. He, M.A. Ratcliff, B.T. Zigler, Effects of gasoline direct injection engine operating parameters on particle number emissions, Energy Fuels 26 (4) (2012) 2014–2027, doi:10.1021/ef201917p.

[19] Q. Wang, C. Yao, Z. Dou, B. Wang, T. Wu, Effect of intake pre-heating and injection timing on combustion and emission characteristics of a methanol fumigated diesel engine at part load, Fuel 159 (2015) 796–802, doi:10.1016/j.fuel.2015.07.032.

[20] M. Saffaripour, T.W. Chan, F. Liu, K.A. Thomson, G.J. Smallwood, J. Kubsh, et al., Effect of drive cycle and gasoline particulate filter on the size and morphology of soot particles emitted from a gasoline-direct-injection vehicle, Environ. Sci. Technol. 49 (19) (2015) 11950–11958, doi:10.1021/acs.est.5b02185.

[21] F. Bonatesta, E. Chiappetta, A. La Rocca, Part-load particulate matter from a GDI engine and the connection with combustion characteristics, Appl. Energy 124 (2014) 366–376, doi:10.1016/j.apenergy.2014.03.030.

[22] S.A. Pfau, A. La Rocca, E. Haffner-Staton, G.A. Rance, M.W. Fay, M. McGhee, Soot in the Lubricating Oil: An Overlooked Concern for the Gasoline Direct Injection Engine?, SAE Technical Paper 2019-01-0301, 2019, doi:10.4271/2019-01-0301.

[23] J. Song, M. Alam, A.L. Boehman, Impact of alternative fuels on soot properties and DPF regeneration, Combust. Sci. Technol. 179 (9) (2007) 1991–2037, doi:10.1080/00102200701386099.

[24] M. Lapuerta, F. Oliva, J.R. Agudelo, A.L. Boehman, Effect of fuel on the soot nanostructure and consequences on loading and regeneration of diesel particulate filters, Combust. Flame 159 (2) (2012) 844–853, doi:10.1016/j.combustflame.2011.09.003.

[25] A. La Rocca, G. Di Liberto, P.J. Shayler, M.W. Fay, The nanostructure of soot-in-oil particles and agglomerates from an automotive diesel engine, Tribol. Int. 61 (2013) 80–87, doi:10.1016/j.triboint.2012.12.002.

[26] C.K. Gaddam, R.L. Vander Wal, Physical and chemical characterization of SIDI engine particulates, Combust. Flame 160 (11) (2013) 2517–2528, doi:10.1016/j.combustflame.2013.05.025.

[27] G. Di Liberto, A. La Rocca, P. Shayler, Computational analysis of the influence of exhaust gas recirculation on the rate of soot transfer to lubricating engine oil, 36th FISITA World Automotive Congress, Korea (2016) September 26–30.

[28] D.M. Stehouwer, G. Shank, S.N. Herzog, C.W. Hyndman, B.G. Kinker, R.P. Simko, Sooted Diesel Engine Oil Pumpability Studies as the Basis of a New Heavy Duty Diesel Engine Oil Performance Specification, SAE Technical Paper 2002-01-1671, 2002, doi:10.4271/2002-01-1671.

[29] H. Sato, N. Tokuoka, H. Yamamoto, M. Sasaki, Study on Wear Mechanism by Soot Contaminated in Engine Oil (First Report: Relation Between Characteristics of Used Oil and Wear), SAE Technical Paper 1999-01-3573, 1999, doi:10.4271/1999-01-3573.

[30] I. Berbezier, J.M. Martin, P. Kapsa, The role of carbon in lubricated mild wear, Tribol. Int. 19 (3) (1986) 115–122, doi:10.1016/0301-679X(86)90016-2.

[31] D. Uy, M.A. Ford, D.T. Jayne, A.E. O'Neill, L.P. Haack, J. Hangas, et al., Characterization of gasoline soot and comparison to diesel soot: morphology, chemistry, and wear, Tribol. Int. 80 (2014) 198–209, doi:10.1016/j.triboint.2014.06.009.

[32] S.A. Pfau, A. La Rocca, E. Haffner-Staton, G.A. Rance, M.W. Fay, R.J. Brough, et al., Comparative nanostructure analysis of gasoline turbocharged direct injection and diesel soot-in-oil with carbon black, Carbon 139 (2018) 342–352, doi:10.1016/j.carbon.2018.06.050.

[33] O. Orhan, E. Haffner-Staton, A. La Rocca, M. Fay, Characterisation of flame-generated soot and soot-in-oil using electron tomography volume reconstructions and comparison with traditional 2D-TEM measurements, Tribol. Int. 104 (2016) 272–284, doi:10.1016/j.triboint.2016.09.015.

[34] E. Haffner-Staton, A. La Rocca, M.W. Fay, Progress towards a methodology for high throughput 3D reconstruction of soot nanoparticles via electron tomography, J. Microsc. (2018), doi:10.1111/jmi.12680.

[35] P.A. Marsh, A. Voet, T.J. Mullens, L.D. Price, Quantitative micrography of carbon black microstructure, Carbon 9 (6) (1971) 797–805, doi:10.1016/0008-6223(71)90013-3.

[36] Á.B. Palotás, L.C. Rainey, C.J. Feldermann, A.F. Sarofim, J.B. Vander Sande, Soot morphology, An application of image analysis in high-resolution transmission electron microscopy, Microsc. Res. Tech. 33 (3) (1996) 266–278 3<266::AID−JEMT4>3.0.CO;2-O, doi:10.1002/(SICI)1097-0029(19960215)33.

[37] A. Sharma, T. Kyotani, A. Tomita, A new quantitative approach for microstructural analysis of coal char using HRTEM images, Fuel 78 (10) (1999) 1203–1212, doi:10.1016/S0016-2361(99)00046-0.

[38] H.-S. Shim, R.H. Hurt, N.Y.C. Yang, A methodology for analysis of 002 lattice fringe images and its application to combustion-derived carbons, Carbon 38 (1) (2000) 29–45, doi:10.1016/S0008-6223(99)00096-2.

[39] A. Galvez, N. Herlin-Boime, C. Reynaud, C. Clinard, J.N. Rouzaud, Carbon nanoparticles from laser pyrolysis, Carbon 40 (15) (2002) 2775–2789, doi:10.1016/S0008-6223(02)00195-1.

[40] K. Yehliu, R.L. Vander Wal, A.L. Boehman, Development of an HRTEM image analysis method to quantify carbon nanostructure, Combust. Flame 158 (9) (2011) 1837–1851, doi:10.1016/j.combustflame.2011.01.009.

[41] Z. Wu, C. Song, G. Lv, S. Pan, H. Li, Morphology, fractal dimension, size and nanostructure of exhaust particles from a spark-ignition direct-injection engine operating at different air–fuel ratios, Fuel 185 (2016) (2016) 709–717, doi:10.1016/j.fuel.2016.08.025.

[42] M. Bogarra, J.M. Herreros, A. Tsolakis, A.P.E. York, P.J. Millington, F.J. Martos, Influence of on-board produced hydrogen and three way catalyst on soot nanostructure in gasoline direct injection engines, Carbon 120 (2017) 326–336, doi:10.1016/j.carbon.2017.05.049.

[43] B. Rohani, C. Bae, Morphology and nano-structure of soot in diesel spray and in engine exhaust, Fuel 203 (2017) 47–56, doi:10.1016/j.fuel.2017.04.093.

[44] M.L. Botero, D. Chen, S. González-Calera, D. Jefferson, M. Kraft, HRTEM evaluation of soot particles produced by the non-premixed combustion of liquid fuels, Carbon 96 (2016) 459–473, doi:10.1016/j.carbon.2015.09.077.

[45] P. Toth, D. Jacobsson, M. Ek, H. Wiinikka, Real-time, in situ, atomic scale observation of soot oxidation, Carbon 145 (2019) 149–160, doi:10.1016/j.carbon.2019.01.007.

[46] P. Toth, A.B. Palotas, E.G. Eddings, R.T. Whitaker, J.S. Lighty, A novel framework for the quantitative analysis of high resolution transmission electron micrographs of soot I. Improved measurement of interlayer spacing, Combust. Flame 160 (5) (2013) 909–919, doi:10.1016/j.combustflame.2013.01.002.

[47] P. Toth, A.B. Palotas, E.G. Eddings, R.T. Whitaker, J.S. Lighty, A novel framework for the quantitative analysis of high resolution transmission electron micrographs of soot II. Robust multiscale nanostructure quantification, Combust. Flame 160 (5) (2013) 920–932, doi:10.1016/j.combustflame.2013.01.003.

[48] C. Wang, T. Huddle, E.H. Lester, J.P. Mathews, Quantifying curvature in high-resolution transmission electron microscopy lattice fringe micrographs of coals, Energy Fuels 30 (4) (2016) 2694–2704, doi:10.1021/acs.energyfuels.5b02907.

[49] C. Wang, T. Huddle, C.-H. Huang, W. Zhu, R.L. Vander Wal, E.H. Lester, et al., Improved quantification of curvature in high-resolution transmission electron microscopy lattice fringe micrographs of soots, Carbon 117 (2017) 174–181, doi:10.1016/j.carbon.2017.02.059.

[50] P. Pré, G. Huchet, D. Jeulin, J.-N. Rouzaud, M. Sennour, A. Thorel, A new approach to characterize the nanostructure of activated carbons from mathematical morphology applied to high resolution transmission electron microscopy images, Carbon 52 (2013) 239–258, doi:10.1016/j.carbon.2012.09.026.

[51] P. Toth, Á.B. Palotás, J. Lighty, C.A. Echavarria, Quantitative differentiation of poorly ordered soot nanostructures: a semi-empirical approach, Fuel 99 (2012) 1–8, doi:10.1016/j.fuel.2012.04.013.

[52] R.C. Gonzalez, R.E. Woods, Digital Image Processing, Prentice Hall, New Jersey, 2002.

[53] J.-O. Müller, D.S. Su, U. Wild, R. Schlögl, Bulk and surface structural investigations of diesel engine soot and carbon black, Phys. Chem. Chem. Phys. 9 (30) (2007) 4018–4025, doi:10.1039/b704850e.

[54] M.L. Botero, Y. Sheng, J. Akroyd, J. Martin, J.A.H. Dreyer, W. Yang, et al., Internal structure of soot particles in a diffusion flame, Carbon 141 (2019) 635–642, doi:10.1016/j.carbon.2018.09.063.

[55] B. Apicella, P. Pré, M. Alfè, A. Ciajolo, V. Gargiulo, C. Russo, et al., Soot nanostructure evolution in premixed flames by high resolution electron transmission microscopy (HRTEM), Proc. Combust. Inst. 35 (2) (2015) 1895–1902, doi:10.1016/j.proci.2014.06.121.

[56] B. Apicella, P. Pré, J.N. Rouzaud, J. Abrahamson, R.L. Vander Wal, A. Ciajolo, et al., Laser-induced structural modifications of differently aged soot investigated by HRTEM, Combust. Flame 204 (2019) 13–22, doi:10.1016/j.combustflame.2019.02.026.

[57] K. Yehliu, R.L. Vander Wal, A.L. Boehman, A comparison of soot nanostructure obtained using two high resolution transmission electron microscopy image analysis algorithms, Carbon 49 (13) (2011) 4256–4268, doi:10.1016/j.carbon.2011.06.003.

[58] C. Russo, A. Ciajolo, Effect of the flame environment on soot nanostructure inferred by Raman spectroscopy at different excitation wavelengths, Combust. Flame 162 (6) (2015) 2431–2441, doi:10.1016/j.combustflame.2015.02.011.

[59] A. Sadezky, H. Muckenhuber, H. Grothe, R. Niessner, U. Pöschl, Raman microspectroscopy of soot and related carbonaceous materials: spectral analysis and structural information, Carbon 43 (8) (2005) 1731–1742, doi:10.1016/j.carbon.2005.02.018.

[60] H.J. Seong, A.L. Boehman, Evaluation of Raman parameters using visible Raman microscopy for soot oxidative reactivity, Energy Fuels 27 (3) (2013) 1613–1624, doi:10.1021/ef301520y.

[61] C.K. Gaddam, C.H. Huang, R.L. Vander Wal, Quantification of nano-scale carbon structure by HRTEM and lattice fringe analysis, Pattern Recognit. Lett. 76 (2016) 90–97, doi:10.1016/j.patrec.2015.08.028.

[62] N. Otsu, A threshold selection method from gray-level histograms, IEEE Trans. Syst. Man Cybern. 9 (1) (1979) 62–66, doi:10.1109/tsmc.1979.4310076.

[63] K. Wan, D. Chen, H. Wang, On imaging nascent soot by transmission electron microscopy, Combust. Flame 198 (2018) 260–266, doi:10.1016/j.combustflame.2018.09.021.

[64] K. Kondo, T. Aizawa, S. Kook, L. Pickett, Uncertainty in Sampling and TEM Analysis of Soot Particles in Diesel Spray Flame, SAE Technical Paper 2013-01-0908, 2013, doi:10.4271/2013-01-0908.

[65] K. Zuiderveld, Contrast limited adaptive histogram equalization, in: P.S. Heckbert (Ed.), Graphics Gems IV, Academic Press, 1994, pp. 474–485, doi:10.1016/B978-0-12-336156-1.50061-6.

[66] M.L. Botero, E.M. Adkins, S. González-Calera, H. Miller, M. Kraft, PAH structure analysis of soot in a non-premixed flame using high-resolution transmission electron microscopy and optical band gap analysis, Combust. Flame 164 (2016) 250–258, doi:10.1016/j.combustflame.2015.11.022.

[67] R.L. Vander Wal, Soot Nanostructure: Definition, Quantification and Implications, SAE Technical Paper 2005-01-0964, 2005, doi:10.4271/2005-01-0964.

[68] P. Thévenaz, U.E. Ruttimann, M. Unser, A pyramid approach to sub-pixel registration based on intensity mailing address, IEEE Trans. Image Process. 7 (1) (1998) 27–41, doi:10.1109/83.650848.

[69] Y. Zhang, R. Zhang, S. Kook, Nanostructure analysis of in-flame soot particles under the influence of jet–jet interactions in a light-duty diesel engine, SAE Int. J. Engines 8 (5) (2015) 2213–2226, doi:10.4271/2015-24-2444.

[70] Z. Xu, X. Li, C. Guan, Z. Huang, Effects of injection timing on exhaust particle size and nanostructure on a diesel engine at different loads, J. Aerosol Sci. 76 (2014) 28–38, doi:10.1016/j.jaerosci.2014.05.002.

[71] K. Al-Qurashi, A.L. Boehman, Impact of exhaust gas recirculation (EGR) on the oxidative reactivity of diesel engine soot, Combust. Flame 155 (4) (2008) 675–695, doi:10.1016/j.combustflame.2008.06.002.

[72] M. Patel, P.B. Aswath, Morphology, structure and chemistry of extracted diesel soot: part II: X-ray absorption near edge structure (XANES) spectroscopy and high resolution transmission electron microscopy, Tribol. Int. 52 (2012) 17–28, doi:10.1016/j.triboint.2012.02.022.